Macromolecules

Article

pubs.acs.org/Macromolecules

How Hollow Are Thermoresponsive Hollow Nanogels?

Janine Dubbert,[†] Tobias Honold,[‡] Jan Skov Pedersen,[§] Aurel Radulescu,[∥] Markus Drechsler,[‡] Matthias Karg,[‡] and Walter Richtering*[,†]

[†]Institute of Physical Chemistry, RWTH Aachen University, 52056 Aachen, Germany

[‡]Physical Chemistry I, University of Bayreuth, 95440 Bayreuth, Germany

[§]Interdisciplinary Nanoscience Center (iNANO) and Department of Chemistry, Aarhus University, 8000 Aarhus, Denmark

[∥]Jülich Centre for Neutron Science, Outstation at MLZ, 85747 Garching, Germany

Supporting Information

ABSTRACT: A main challenge in colloid science is the development of smart delivery systems that store and protect actives from degradation and allow release in response to an external stimulus like temperature. Hollow nanogel capsules made of temperature-sensitive polymers are particularly promising materials. The stimuli-sensitive void size, shell thickness, and permeability determine cargo storage and its release behavior. Thus, determination and control of these morphological parameters are of outmost relevance for the design of new, functional drug delivery vehicles. Here we investigate quantitatively void size and shell thickness of hollow nanogels at different states of swelling by means of small-angle neutron scattering (SANS) employing contrast variation. We demonstrate the structure-sensitivity dilemma: hollow nanogels with a slightly cross-linked shell reveal distinct temperature sensitivity but possess nearly no void (14% of the initial core volume) and are thus hardly "hollow". Nanogels with a stiff shell are indeed hollow (albeit with smaller void as compared to the core size of the template) but less temperature sensitive.

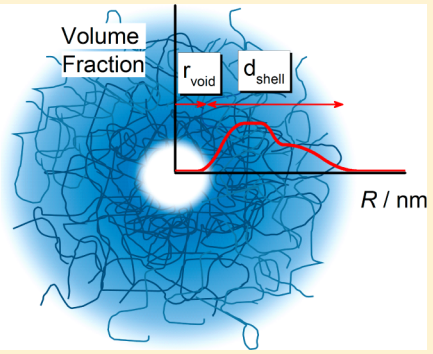

INTRODUCTION

Hollow capsules are in the focus of the rational design of responsive drug delivery systems for applications in the biomedical field.[1−5] Smart drug delivery systems store and protect drugs from degradation *in vivo* but allow drug release e.g. in response to an external stimulus.[6−11]

Microfluidic techniques allow for the fabrication of monodisperse microcapsules with rather large sizes.[12,13] The geometry of the premicrogel droplets determines the particle geometry. Controlling the morphology is either achieved via aligned glass microcapillaries[14] or elastomer-based devices[15] that are replicated from master molds allowing the fabrication of particles with varying morphologies. However, up to now the technique is restricted to the preparation of comparably large particles of 10−100 μm.

Slightly smaller particles can be achieved through a layer-by-layer deposition technique where oppositely charged polyelectrolytes are deposited on a colloidal template.[16,17] The number of deposited layers determines the shell thickness accordingly. Capsules are formed if the core is subsequently chemically removed. However, the formation of thick shells can be rather tedious, and the multilayer shell can become unstable e.g. with increasing salt concentration unless the layers are chemically cross-linked.[18−21]

Nanocapsules with a permeable chemically cross-linked shell can be prepared by encapsulating a sacrificial core by a shell of a cross-linked swollen polymer network.[22] Silica particles have proven to be a suitable core material. They can be routinely prepared in a Stoeber synthesis[23] and require a linking agent to chemically connect the polymer shell around the silica core.[22] Afterward, the core is dissolved, which leads to the formation of pitted particles that typically are assumed to be hollow with the void size being given by the size of the sacrificial core.

Hollow nanoparticles made of temperature-sensitive polymers like poly(*N*-isopropylacrylamide) (PNIPAM) are particularly promising materials and have been prepared based on this approach.[24−28] The volume phase transition temperature (VPTT) of PNIPAM microgels in water is 32 °C and can be tailored for specific applications by incorporating suitable comonomers.[29−32] Recently, we reported on hollow nanogels with two temperature-sensitive shells.[33]

Obviously, controlling the stimulus-dependent void size and shell thickness is crucial for the rational design of new, functional drug delivery vehicles.[13,34,35] However, a quantitative determination of the void size and its dependence on the stimulus is challenging and has not been reported before.

In this contribution we present a small-angle neutron scattering (SANS) study including a detailed contrast variation series to reveal the structure of the core−shell and hollow nanogels quantitatively. A form factor model for core−shell particles was evolved, and a global fit of the SANS curves was performed to obtain the high quality data. The SANS analysis is

Received: October 7, 2014
Revised: November 21, 2014
Published: December 9, 2014

complemented with electron microscopy images, and the swelling of the particles is analyzed via dynamic light scattering measurements.

EXPERIMENTAL DETAILS

Preparation of Core−Shell Particles. The core−shell particles have been prepared in a seed and feed synthesis. The detailed synthesis protocol was adopted from the literature.[36] Briefly, silica nanoparticle cores were synthesized first by mixing 130 mL of ethanol (absolute) and 11 mL of ammonia solution in a three-neck round-bottom flask equipped with a reflux condenser. The solution was heated to 50 °C under continuous stirring with a magnetic stirrer. After approximately 10 min of equilibration time at 50 °C a solution of 5 mL of tetraethyl orthosilicate (TEOS) in 15 mL of ethanol (absolute) was added quickly. After 12 h of reaction time, the surface of the silica nanoparticles was functionalized with methacryloxypropyl-trimethoxysilane (MPS) to introduce reactive functionalities (double bonds) for the following polymerization. The particle concentration was increased by a factor of 10 to obtain a seed stock solution through subsequent purification via centrifugation. For particle type CS-1 one-fourth of the pretreated core stock solution was added to a degassed mixture of NIPAM (537 mg), *N*,*N*-methylenebis(acrylamide) (BIS) (39.4 mg (5.4 mol %)), and PVP (1 mg/mL) in water (100 mL). For CS-2 the same masses of monomer and cross-linker were used in a 200 mL synthesis with double amounts of silica seed particles and PVP as in the synthesis of CS-1. CS-3 was synthesized with 241 mg of NIPAM and 59.1 mg of BIS in 100 mL of water (18 mol % BIS). In all three syntheses solutions of 10 mg of KPS in 1 mL of water were added to initiate the polymerizations. Centrifugation was applied to purify the particles from unreacted monomer and short chain oligomers. Afterward, the core−shell particles were lyophilized for storage and further applications.

Preparation of pitted particles: The particles were pitted by treatment with highly diluted HF as previously reported in the literature.[24,27,37,38] Briefly, freeze-dried core−shell particles were dispersed in 7.5 mL of bidistilled water, and 10 droplets of hydrofluoric acid (40%) were added. The mixture was stirred overnight and subsequently dialyzed against water until a neutral pH was reached. Zha et al. reported that infrared spectroscopy data confirmed that the amide linkages are not damaged under these conditions.[24] The successful core dissolution has been proven by means of electron dispersive X-ray measurements.

Dynamic light scattering (DLS) measurements were performed to determine the hydrodynamic radii (R_h) of core, core−shell, and pitted particles. For all measurements an ALV setup with a goniomer (ALV 5000) and a HeNe laser with a wavelength of 633 nm was applied. The temperature of the toluene index match bath was controlled via an external programmable thermostat (Julabo F32). All samples were highly diluted to avoid multiple scattering. For each temperature, measurements were performed at three different scattering angles to determine the mean diffusion coefficient of the system from the linear regression of the decay rate Γ versus the square of the scattering vector q. From the diffusion coefficient the hydrodynamic radius R_h is calculated via the Stokes−Einstein equation.

SANS measurements were carried out at the instrument KWS 2 at the Heinz Maier-Leibnitz institute in Garching, Munich. Measurements were performed at wavelength of 5 and 18 Å with a wavelengths spread of 20%. The sample concentration was 0.2 or 1 wt %, respectively. All data were corrected for background and empty cell scattering and calibrated to absolute scale by PMMA scattering using the standard procedure of the instrument. The resulting intensity is displayed as a function of the modulus of the scattering vector, q.

Cryo-TEM samples were prepared by vitrification of thin liquid films (2 μL) supported on lacey carbon film copper grids (Science Services, Munich), which were hydrophilized by air plasma glow discharge (30 s with 50 W, Solarus 950, Gatan, Munich, Germany). The shock freezing was done with liquid ethane using a temperature-controlled freezing unit (Zeiss Cryobox, Carl Zeiss Microscopy GmbH, Jena, Germany). The temperature was monitored and kept constant in the chamber during all steps of preparation. The sample specimen was inserted into a cryo-transfer holder (CT3500, Gatan, Munich, Germany) and transferred to a Zeiss EM922 Omega EFTEM microscope (Zeiss Microscopy GmbH, Jena, Germany). The microscope was operated at an acceleration voltage of 200 kV. Examinations of the sample were carried out at temperatures around 90 K. Zero-loss filtered images (ΔE = 0 eV) were taken under reduced dose conditions (100−1000 e/nm^2). All images were registered digitally by a bottom mounted CCD camera system (Ultrascan 1000, Gatan, Munich, Germany) combined and processed with a digital imaging processing system (Digital Micrograph GMS 1.9, Gatan, Munich, Germany).

Theoretical Background and Data Analysis. Small-angle neutron scattering (SANS) experiments yield information on the intensity distribution $I(q)$ as a function of the momentum transfer q in reciprocal space. For suspensions of spherical, monodisperse particles the differential cross section $d\sigma(q)/d\Omega$ is a common way to express $I(q)$:

$$\frac{d\sigma}{d\Omega}(q) = nP(q) \tag{1}$$

$P(q)$ represents the form factor and n the particle number density. A significant instrumental smearing of the measurement data occurs in SANS experiments that depends on setup geometry, wavelength distribution, and the detector resolution. It is taken into account by introducing a resolution function $R(\langle q\rangle,q)$ that describes the probability distribution for the scattering vector q for a given nominal scattering vector $\langle q\rangle$.

$$I^{\mathrm{mod}}(\langle q\rangle) = n\int_0^\infty R(\langle q\rangle, q)\frac{d\sigma}{d\Omega}(q)\, dq \tag{2}$$

The core−shell particles that were investigated in this study consist of a silica core and a cross-linked PNIPAM shell. It was shown before that due to the higher reaction rate of BIS compared to PNIPAM a graded interface to water is formed during the polymerization of a pure PNIPAM microgel. We assume that the same behavior occurs during the synthesis of the shell in silica-core−PNIPAM-shell particle synthesis. Thus, we applied a model based on the model form factor expression of Berndt, Pedersen, and Richtering[39] with minor extensions that will be explained below. The density profile that depicts this model is shown in Figure 1.

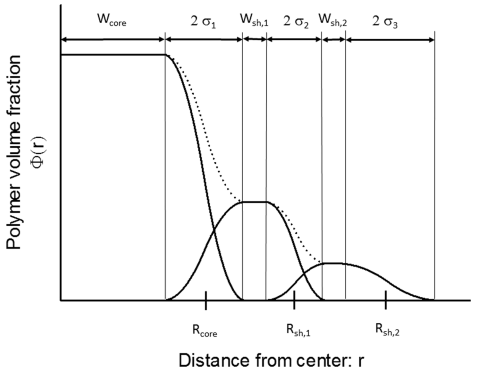

Figure 1. Schematic representation of the core−shell model based on the model by Berndt, Pedersen, and Richtering.[39] The central core has a constant volume fraction up to $r = W_{core}$ and a graded interface with a half-high radius of $R_{core} = W_{core} + \sigma_1$, where σ_1 describes the width of the interface. The first shell has a grading of the inner interface given by σ_1, a constant volume fraction in a range $W_{sh,1}$, and a graded outer interface with a width given by σ_2. The interface between the first shell and the second (half-height) is located at $r = W_{core} + 2\sigma_1 + W_{sh,1} + \sigma_2$. The second shell has a grading of the inner interface given by σ_2, a constant volume fraction in a range $W_{sh,2}$, and a graded outer interface with a width given by σ_3. The interface between the second shell and the solvent (half-height) is located at $r = W_{core} + 2\sigma_1 + W_{sh,1} + 2\sigma_2 + W_{sh,2} + \sigma_3$.

dx.doi.org/10.1021/ma502056y | Macromolecules 2014, 47, 8700−8708

The density profile is based on a profile with a constant density in the center in a region up to $r = W$ and a decay of the outer surface, which is determined by σ. In agreement with the previous work, the interfaces are piecewise described by parabolic functions. The radial density profile $\rho(r)$ of a particle with such a graded surface is expressed by the half-height radius $R = W + \sigma$ is

$$\rho(r) = 1 \quad r \le (R - \sigma) \tag{3a}$$

$$\rho(r) = 1 - \frac{1}{2}\frac{[(r - R) + \sigma]}{\sigma^2} \quad (R - \sigma) < r \le R \tag{3b}$$

$$\rho(r) = \frac{1}{2}\frac{[(R - r) + \sigma]^2}{\sigma^2} \quad R < r \le (R + \sigma) \tag{3c}$$

$$\rho(r) = 0 \quad (R + \sigma) < r \tag{3d}$$

The volume of the particles that this profile describes is $V = 4\pi V_n$, where $V_n = R^3/3 + R\sigma^2/6$.

The Fourier transformation of this scattering profile leads to the scattering amplitude $\Phi(q,R,\sigma)$:

$$\Phi(q, R, \sigma) = \frac{1}{V_n}\left[\left(\frac{R}{\sigma^2} + \frac{1}{\sigma}\right)\frac{\cos(q(R + \sigma))}{q^4} + \left(\frac{R}{\sigma^2} - \frac{1}{\sigma}\right) \times \frac{\cos(q(R - \sigma))}{q^4} - \frac{3\sin(q(R + \sigma))}{q^5\sigma^2} - \frac{3\sin(q(R - \sigma))}{q^5\sigma^2} + \frac{2\cos(qR)}{q^5\sigma^2} + \frac{6\sin(qR)}{q^5\sigma^2}\right] \tag{4}$$

This expression is normalized to $\Phi(q = 0, R, \sigma) = 1$ so that the scattering amplitude of the core with radius R_{core} and interface width σ_1 is (cf. Figure 1 for definition of parameters for the profile)

$$A_{core}(q, R_{core}, \sigma_1, \Delta\rho_{core}) = \Delta\rho_{core} V_{core} \Phi_{core}(q, R_{core}, \sigma_1) \tag{5}$$

where $\Delta\rho_{core}$ and V_{core} are respectively the scattering length density and the volume of the core.

The scattering amplitude of the first shell is in the usual way given by differences of scattering amplitudes (4) with different radii and interface width:

$$A_{sh,1}(q, R_{sh,1}, \sigma_2, \Delta\rho_{sh,1}, R_{core}, \sigma_1) = \Delta\rho_{sh,1}(V_{sh,1}\Phi(q, R_{sh,1},\sigma_2) - V_{core}\Phi(q, R_{core}, \sigma_1)) \tag{6}$$

where $\Delta\rho_{sh,1}$ and $V_{sh,1}$ are respectively the scattering length density and the volume that correspond to a particle with $R_{sh,1}$ and σ_2 related to the first shell. Similarly, the scattering amplitude of the second shell is

$$A_{sh,2}(q, R_{sh,2}, \sigma_3, \Delta\rho_{sh,2}, R_{sh,1}, \sigma_2) = \Delta\rho_{sh,2}(V_{sh,2}\Phi(q, R_{sh,2},\sigma_3) - V_{sh,1}\Phi(q, R_{sh,1}, \sigma_2) \tag{7}$$

where $\Delta\rho_{sh,2}$ and $V_{sh,2}$ are respectively the scattering length density and the volume that correspond to a particle with $R_{sh,2}$ and σ_3 related to second shell. The scattering amplitude of the full particle with core and two shells is then

$$A(q) = A_{core}(q, R_{core}, \sigma_1, \Delta\rho_{core}) + A_{sh,1}(q, R_{sh,1}, \sigma_2, \Delta\rho_{sh,1}, R_{core}, \sigma_1) + A_{sh,2}(q, R_{sh,2}, \sigma_3, \Delta\rho_{sh,2}, R_{sh,1}, \sigma_2) \tag{8}$$

The square of the scattering length amplitude $A^2(q)$ equals the form factor $P(q)$. The model described above is versatile. It is able to describe core and shells with varying morphologies, e.g., solid sphere-like or microgel-like, with decaying polymer density at the surfaces.

To take the polydispersity of core radius and polymer shell thickness into account, it was described by a normalized Gaussian number distribution of a scale factor:

$$D(S, \langle S\rangle = 1, \sigma_{poly}) = \frac{1}{\sqrt{2\pi\sigma_{poly}^2\langle S\rangle^2}} \exp\left(-\frac{(S - \langle S\rangle)^2}{2\sigma_{poly}^2\langle S\rangle^2}\right) \tag{9}$$

$\langle S\rangle = 1$ is the average scale factor of the size, and σ_{poly} denotes the relative particle size polydispersity. Better fits could be obtained if the polydispersity of the polymer layer thickness was larger than that of the core. Therefore, the polydispersity was increased by a constant factor for the shell thickness. This constant factor was optimized in the least-squared fits.

The internal structure of the microgel layer was described by a Lorentzian function $I_L(q) = I_L(0)/[1 + q^2\xi^2]$ that is added to $P(q)$. Herein the average correlation length in the network is described by ξ. $I_L(q)$ contributes significantly to the intensity in the high-q range for the swollen samples. Finally, a constant background I_{back} is included to correct for residual incoherent scattering, mainly from the solvent.

Summarizing all the above-mentioned contributions yields a model expression for the scattering intensity distribution

$$I^{mod}(\langle q\rangle) = n\int_0^\infty\int_0^\infty R(\langle q\rangle, q)D(S, \langle S\rangle, \sigma_{poly}) \times [A^2(q) + I_L(q) + I_{back}]\, dS\, dq \tag{10}$$

with the number density

$$n = c\left[\int_0^\infty [\phi_{core}\rho_{core}V_{core} + \phi_{sh,1}\rho_{sh,1}(V_{sh,1} - V_{core}) + \phi_{sh,2}\rho_{sh,2}(V_{sh,2} - V_{sh,1})]D(S, \langle S\rangle, \sigma_{poly})\, dS\right]^{-1} \tag{11}$$

where c represents the polymer mass concentration, ϕ_i and ρ_i are respectively the volume fraction and the partial specific mass density of the ith component, and the volumes have implicitly a dependence on the structural parameters as explained above. Note that these parameters and the volume fractions are fit parameters, when the model is fitted to the experimental SANS data. The scattering length density of the silica core (3.47×10^{-6} 1/Å^2) and the PNIPAM shell (8.69×10^{-7} 1/Å^2) were calculated with the SLD calculator provided by NIST.[40]

The described model was fitted to the experimental data using a least-squares routine to a reduced χ^2 criterium. Both the individual contrasts and the complete contrast variation series, in which the H_2O and D_2O composition of the solvent were varied, were fitted. In the contrast variation series the structure of the particles was the same for all contrasts, and the excess scattering length of each component of the model was calculated using the composition of the solvent. The scattering length density of the various components of the model are then given by the excess scattering length density multiplied by the volume fraction of the component.

The radial profiles in terms of material volume fraction can be plotted using the expressions 3a−3d taking appropriate differences as for the scattering amplitudes and multiplying the various components by their volume fraction. However, we used another approach based on numerical Fourier transformation of the scattering amplitude using volume fractions and omitting scattering length densities. This gives the radial volume fraction profiles in real space as

$$\rho(r) = \frac{1}{2\pi^2}\int A(q)\frac{\sin(qr)}{qr}q^2\, dq \tag{12}$$

RESULTS AND DISCUSSION

Figure 2 shows a schematic depiction of the system under investigation and the relevant length scales: Pitted particles were obtained after dissolution of silica cores from silica−PNIPAM core−shell colloids using hydrofluoric acid (HF). The overall dimensions of the core−shell colloids ($2r_{total}$) are determined by the core diameter ($2r_{core}$) and the thickness of the chemically cross-linked PNIPAM shell ($2d_{shell}$). The dissolution of the silica core creates a void volume in the

dx.doi.org/10.1021/ma502056y | Macromolecules 2014, 47, 8700−8708

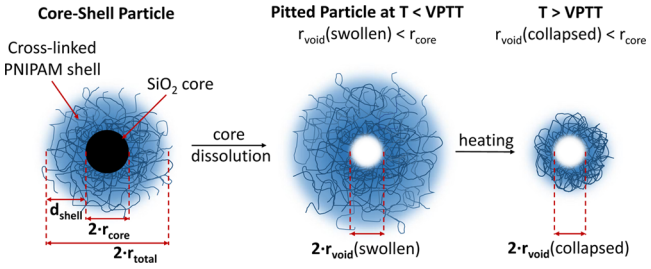

Figure 2. Schematic representation of the core–shell particles and the pitted "hollow" particles after core dissolution.

interior particle. Depending on the elasticity of the polymer network, additional swelling of the PNIPAM might occur, reducing the void volume as compared to the original silica core volume, leading to $r_{void} < r_{core}$.

In order to study the effect of network elasticity and network dimensions on the void volume, we prepared pitted particles from core–shell systems with three different shells of varying cross-linker content and shell thickness: CS-1 and CS-2 contain silica cores from the same batch and vary in shell thickness achieved through different silica/monomer ratios during the preparation (see Experimental Details section for further information). CS-3 shows a comparable shell thickness as CS-2, but the cross-linker/monomer ratio used in the polymerization of the shell was 3 times as high in comparison to CS-1 and CS-2. For CS-3 a slightly smaller silica core was used.

The successful removal of the silica cores was studied by cryo-TEM. Figure 3 shows cryo-TEM images of the core–shell particles CS-1 (a1, a2) and the respective pitted particles PP-1 (b1, b2) obtained from vitrification of dilute aqueous particle dispersions at room temperature (swollen state). The core–shell morphology of the particles prior to HF treatment is clearly visible in Figure 3, a1 and a2. Because of the significantly larger electron density of the silica core, the core is observable within the PNIPAM network. After HF treatment (b1, b2), the contrast of the overall particles is rather low since the electron density of the structure is now solely given by the polymer shell. In particular, the higher magnification shown in (b2) reveals that the silica core has been removed. Complete removal of the silica core has also been proven by EDX analysis.

However, the low contrast of the PNIPAM network in electron microscopy hampers an unambiguous analysis of the overall particle size and more importantly of the void size. The images shown in Figure 3b do not provide clear evidence whether or not the pitted particles are in fact hollow.

The overall particle dimensions and the swelling behavior of the core–shell and pitted particles were studies using dynamic light scattering. This technique is perfectly suited to obtain ensemble average, statistically relevant values of particle overall dimensions from aqueous dispersion and hence under conditions which are of actual relevance for drug delivery purposes. The diffusion coefficient is determined from the mean relaxation rate (measured at various scattering angles), and the hydrodynamic radius is obtained via the Stokes–

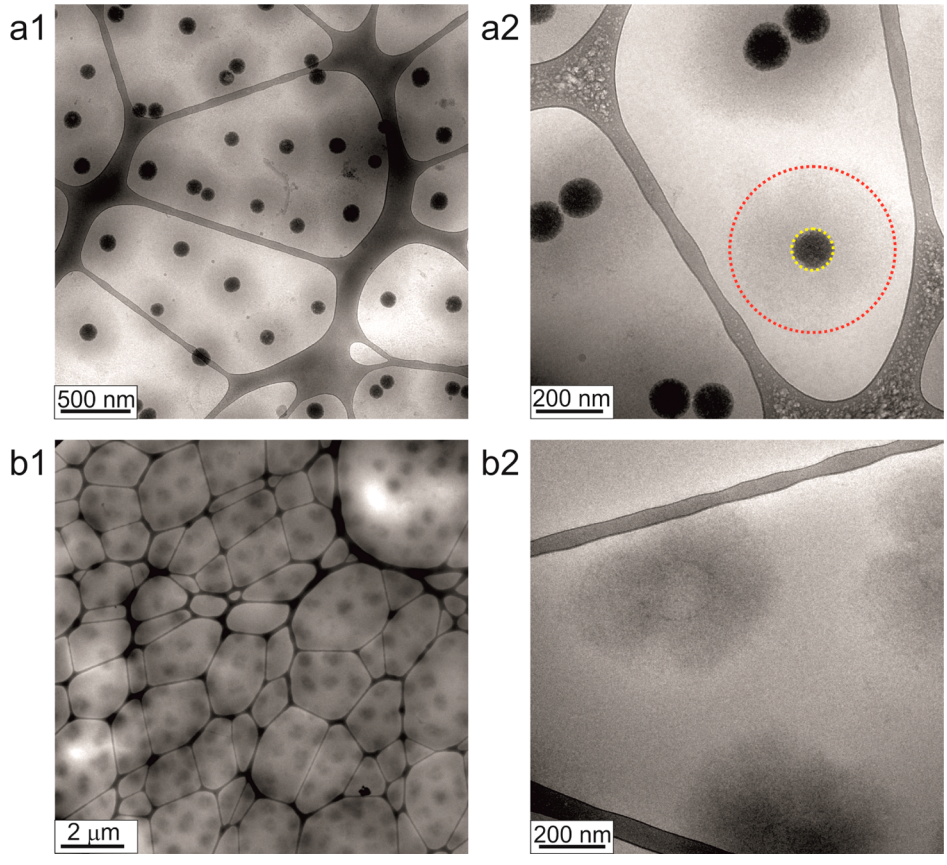

Figure 3. Cryo-TEM images of CS-1 at low (a1) and high magnification (a2) before HF treatment. The red and yellow dotted circles in (a2) highlight the overall dimensions and the core, respectively. Cryo-TEM images of PP-1 at low (b1) and high magnification (b2). Samples were prepared from dilute aqueous dispersion at room temperature by vitrification using liquid ethane.

dx.doi.org/10.1021/ma502056y | *Macromolecules* 2014, 47, 8700–8708

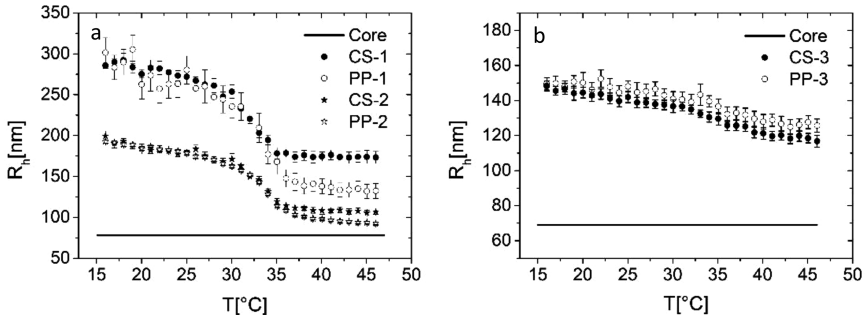

Figure 4. Results from temperature-dependent dynamic light scattering measurements of the core−shell (full symbols) and the pitted particles (open symbols). The temperature-independent size of the silica core is indicated by the horizontal lines.

Einstein equation. Figure 4 shows the evolution of hydrodynamic radius with temperature for all three systems.

All samples reveal a temperature-sensitive size. Systems 1 and 2 (Figure 4a) show the expected volume phase transition behavior with transition temperatures in the order of 32−33 °C, and the VPTT is not affected by the dissolution of the silica core. The higher degree of cross-linking for system 3 (Figure 4b) results in a significantly lower degree of swelling and in a loss of the sharp transition at 32 °C. The difference in shell thickness for CS-1 and PP-1 compared to CS-2 and PP-2 is clearly visible as the hydrodynamic radii for system 1 are larger at every investigated state of swelling.

At low temperatures, the size of the pitted particles is similar to that of the parent core−shell particles for all three systems. This indicates that the dissolution of the silica core does not lead to additional swelling of the PNIPAM network to the *exterior*. However, differences between the hydrodynamic radii of core−shell and pitted particles respectively are observed for systems 1 and 2 at temperatures above the VPTT: The pitted particles are smaller than the parent core−shell particles, indicating that PNIPAM network collapses into the *interior*, i.e., into the "void" space, previously occupied by the silica core.

Again, system 3 behaves differently: The high cross-linker content restricts the swelling of the PNIPAM so strongly that core−shell and pitted particle show nearly identical hydrodynamic size even in the collapsed state.

However, DLS measurements solely provide information about the overall dimensions of the particles. The inner structure and spatial distribution of polymer segments inside the shell cannot be determined with this technique.

Therefore, the internal structure was investigated by SANS at different scattering contrasts. First of all, a detailed contrast variation series was performed for CS-2. The core−shell particles were investigated in seven different D_2O/H_2O mixtures at 20 °C (Figure 5). On the basis of this series of measurements the form factor model was evolved and applied to the data shown in Figure 5. The lines in the plot represent the fits.

A qualitative comparison of the form factor measurements in different D_2O/H_2O compositions shows that the characteristics of the scattering curve clearly depend on the solvent composition. Starting from the measurement in pure D_2O (black curve) the form factor minimum shifts because the contributions from silica core and PNIPAM shell, respectively, change differently when the D_2O/H_2O ratio in the solvent is varied. To confirm the calculated match point for silica of 3.47×10^{-6} 1/Å^2 (≙ 58 wt % D_2O and 42 wt % H_2O), we extracted the intensity at a distinct q-value for the particles in all measured solvent compositions. The minimum of a parabola fit

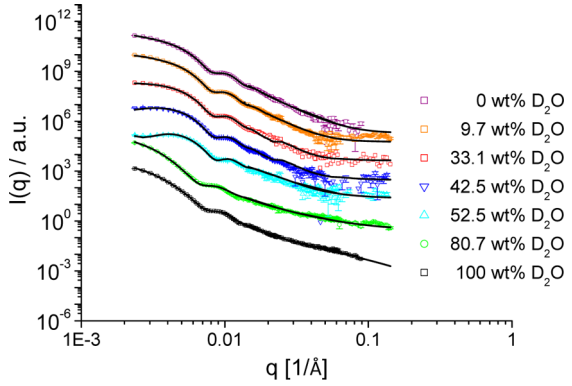

Figure 5. Contrast variation series for CS-2 particles measured at 20 °C in H_2O/D_2O mixtures. The intensities of scattering curves and fits are shifted for clarity reasons. The lines represent the model fits to the scattering data.

yields the point of zero average contrast (ZAC point) (compare Figure S1 in the Supporting Information). The measured value corresponds to a composition of 62 wt % D_2O and 38 wt % H_2O and is thus in good agreement with the calculated value. The deviation of calculated and measured value lies within the error of the measurement.

To obtain structural details, the contrast variation data set was fitted simultaneously with the extended core−shell form factor model as described in the Experimental Details section. The fact that all contrast situations can be fitted with that model simultaneously (compare Figure 5) with high accuracy shows that we found a structure that reflects the core−shell morphology realistically. Figure 6 shows the resulting density profile from the form factor analysis of the contrast variation series measured for CS-2 at 20 °C.

The core region is described by a box profile as obtained from the fit of the pure core measurement. Surprisingly, we found that a dense layer of PNIPAM near the silica particle surface is necessary to describe the shell at all contrasts appropriately. This is a distinct difference to PS-core−PNIPAM-shell systems on the one hand and core−shell microgels which were also analyzed by means of small-angle scattering previously.[39,41,42] The dense polymer layer in our system has a volume fraction of up to 40%, which is rather high for a microgel in the swollen state. We assume that the dense polymer layer results from the surface modification of the silica particles. In this step a monolayer of molecules with reactive double bonds are attached to the particles from which polymerization can start and a rather dense polymer region can form. The outer region of the shell is described by a

dx.doi.org/10.1021/ma502056y | *Macromolecules* 2014, 47, 8700−8708

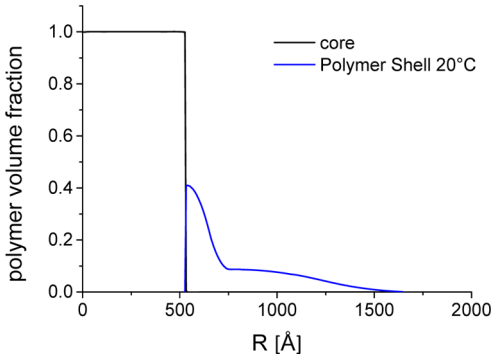

Figure 6. Radial density profile that describes the CS-2 particle morphology at T < VPTT obtained from the form factor model fit.

polymer layer that decays from about 10% volume fraction to zero at the surface of the particle.

Additionally, the structure of the core−shell particles at temperatures above the VPTT was analyzed at three different contrasts, and the form factors were analyzed in accordance to the low-temperature measurement (see Figure 7).

For conventional PNIPAM microgels above the VPTT the structure can be approximated with a polydisperse hard-sphere-like model. The optimum fits for our system at high temperature were obtained for a box profile that again describes the core in the center of the particle. The collapsed polymer shell can also be described with a single box profile of constant polymer density, despite the bilayered structure that was necessary to describe the swollen shell.

Furthermore, we investigated the systems CS-1 and CS-3 at two contrasts, namely at the scattering length density match point of the core (62.6 wt % D_2O in the D_2O/H_2O mixture) and in pure D_2O. Additionally, the pitted particles were studied in D_2O. Thus, the thickness of the shell as well as the density of polymer segments inside the shell can be determined for the systems dependent on cross-linking density and shell thickness. The scattering curves are presented in Figure 8a,b, and the results of the fits are summarized in Table S1 of the Supporting Information.

In the case of low cross-linker concentration (CS-1 and CS-2) the scattering curves of the pitted particles and the core−shell particles differ both above (Figure 8, row a) and below (Figure 8, row b) the VPTT. The positions of the form factor minima of the pitted particles are shifted to higher q values as compared to the core−shell particles at both temperatures, which indicates that the structure of the PNIPAM shell is different. This effect is less pronounced for CS-3/PP-3, which reflects that the higher cross-linker content restricts the swelling of the shell after core dissolution.

Furthermore, the form factor minima are less pronounced for the pitted particles in the swollen state compared to the core−shell particles. In principle, the smearing of the minima could originate from increased polydispersity. However, the size polydispersity should not change by dissolving the silica cores. It is known for swollen PNIPAM microgels that the smearing of the form factor minima is due to a smooth decay of segment density at the surface.[43] This behavior is typical for colloidal PNIPAM and originates from the inhomogeneous spatial distribution of the cross-linker. This is because the cross-linker reacts faster than NIPAM during precipitation polymerization, which leads to a preferential incorporation of the cross-linker at the beginning of the reaction.[44,45]

The qualitative analysis of the scattering curves already indicates structural changes in the polymer shell after dissolution of the silica core. The scattering curves were fitted with form factor models, and density profiles were calculated in order to provide a quantitative description of the temperature-dependent structure of the shell. These form factor fits are shown as solid lines in Figure 8a,b.

The scattering data of the core−shell particles in the collapsed state (50 °C) can be described with a core−shell model that consists of a box profile for the core as well as for the shell with a sharp interface at the particle surface (see Figure 8, row c). At 20 °C, the rigid silica core still has a box profile; however, the density of swollen polymer shell cannot be described with a simple model of a smoothly decaying polymer density, as already discussed before in more detail.

Next, we discuss the structure of the pitted particles, which was also analyzed by means of SANS above and below the VPTT. In the collapsed state a box profile with sharp interfaces describes the scattering data with high accuracy (see dashed lines in Figure 8a,c). However, it is important to notice that the size of the void is diminished compared to the initial silica core. Obviously, the collapsed polymer shell intrudes the void and fills most of the volume previously occupied by the silica core. Again, this effect is less pronounced for the highly cross-linked species PP-3.

The situation in the swollen state is even more complex. The polymer shell swells into the void and occupies a large fraction of the free space gained from the dissolution of the silica core. The PNIPAM shell reveals a complex density profile. The expansion of the PNIPAM shell on the *outside* seems to restrict the swelling of the polymer shell into the void. In the case of

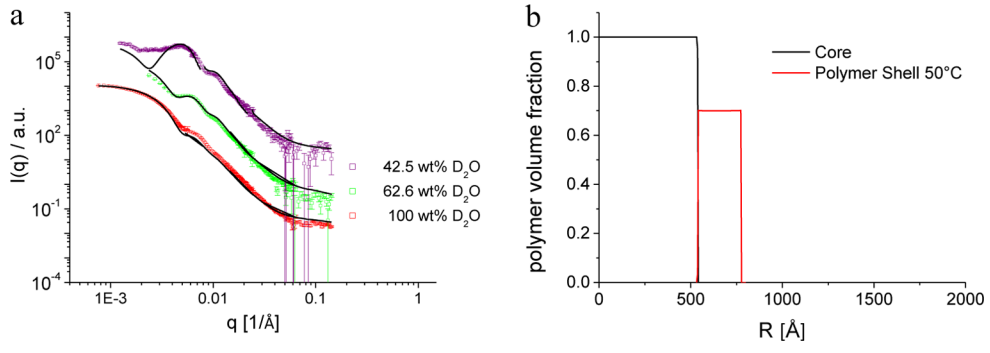

Figure 7. (a) Form factor measurements of CS-2 particles and corresponding fits of the core−shell microgels above the VPTT. (b) Resulting density profiles from the fits to the core−shell model.

dx.doi.org/10.1021/ma502056y | *Macromolecules* 2014, 47, 8700−8708

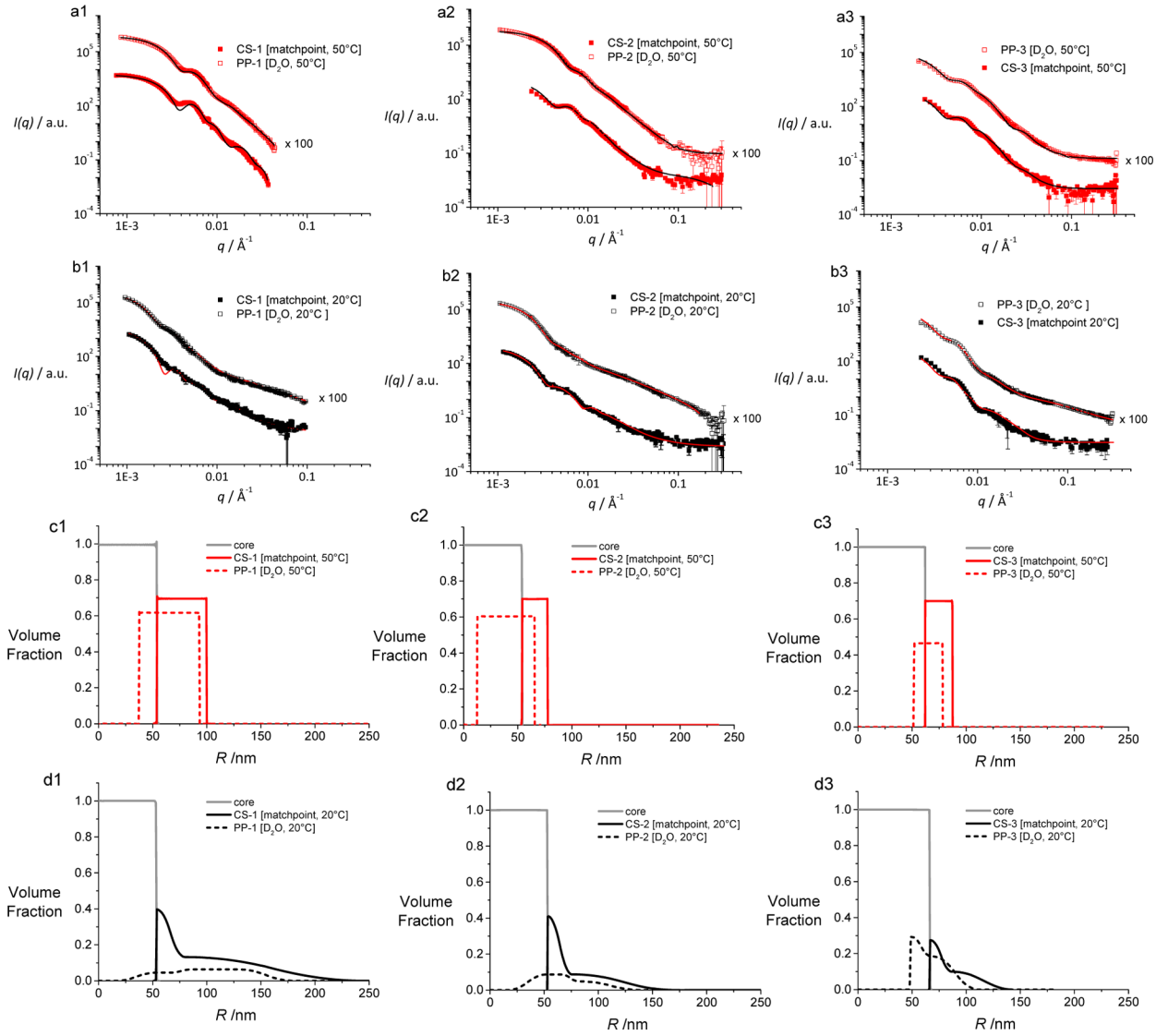

Figure 8. Experimental SANS scattering profiles of the core−shell particles in a mixture of 62.6 wt % D_2O and 37.4 wt % H_2O (closed symbols) and of the pitted particles in D_2O (open symbols) at 50 °C (a) and 20 °C (b). The scattering curves of the pitted particles are vertically shifted by a factor of 100 for the sake of clarity. The solid lines are fits according to the form factor model. The corresponding radial density profiles calculated from the modeling procedure are shown in (c) for T > VPTT and (d) T < VPTT. Note that in the case of all pitted particles the void is much smaller than the original silica template core at both temperatures. The polymer shell swells into the void after the core is dissolved. This effect is less pronounced at high cross-linking densities (PP-3).

PP-3 the shape of the density profile with two regions of different densities inside the shell is very pronounced. The shape of the profile is comparable to the shell profile before the dissolution of the core. Still, the shell intrudes the void but to a much smaller extent as compared to the other two systems.

Different hollow polymer particle systems were reported during the past years. Rather large particles can be prepared with microfluidic, interfacial polymerization or layer by layer techniques.[12,13,46,47] For these particles with voids sizes in the micrometer size range a swelling of the shell to the inside, which diminishes the void size on the nanometer scale, can be assumed as marginal. The swelling to the inside is, however, of great importance for smaller capsules with sizes in the nanometer range that are comparable to the system investigated in this study. So far, electron microscopy images and atomic force microscopy were used to characterize hollow spheres with temperature responsive shell.[24,26,27,48−51] These techniques cannot provide quantitative data on the void size, shell thicknesses, and polymer densities as derived from the SANS measurements and form factor analysis in this study. However, only a detailed knowledge of these properties allows to tailor systems that exhibit e.g. distinct loading and release properties or that shall host smaller nanoparticles in the void.[52]

The quantitative analysis of the SANS data obtained at different scattering contrasts demonstrates unambiguously that the polymer-free, "hollow" void inside the pitted particles is much smaller than the size of the original silica core. The pitted particles have indeed a central region that is free of polymer and can be called "hollow". However, as long as the cross-linker content is low the void is rather small. The volume of the void is only 14% of the core volume at 20 °C and only 5% of the core volume at T > VPTT for the CS-2 system. For the highly cross-linked system, the void is still smaller compared to the initial core volume (31% at 20 °C and 38% at 50 °C), but the effect is less dramatic. However, the unique temperature-

dx.doi.org/10.1021/ma502056y | Macromolecules 2014, 47, 8700−8708

sensitive, "smart" behavior of PNIPAM[53] is only pronounced for particles with lower cross-linker contents.

This illustrates the structure-sensitivity dilemma of responsive hollow nanogels: Preparing hollow nanogels with a significantly large void requires a stiff shell of cross-linked polymer; a stiff shell, however, is hardly stimuli-sensitive. With higher cross-linker ratios the soft-sphere-like behavior of PNIPAM becomes less pronounced, and the polymer network is more rigid.[54,55] However, it is exactly this softness and strong responsiveness of PNIPAM to temperature that make hollow temperature-sensitive polymer particles attractive for applications.[1,56] In addition, increasing the cross-linking will decrease the shell permeability due to a reduced mesh size. Obviously, a compromise between void size, sensitivity, and shell permeability has to be chosen when designing hollow carrier systems.

Our observations that (i) the void of the hollow particles is significantly smaller than the size of the original core and (ii) the density profile of the polymer shell is affected by core removal need to be taken into account if such hollow particles are to be tailored for distinct applications.[1,6,10,57] If the void shall be filled with e.g. small particles, the loading capacity of a pitted particle is restricted by the accessible void volume in the center of the polymer particle.[34,58]

In conclusion, we have presented a study on the structure of temperature-sensitive silica−PNIPAM core−shell systems and the corresponding pitted particles after core dissolution. A detailed contrast variation measurement series revealed the structure of the core−shell particles. A dense layer of PNIPAM near the silica particle surface was found, which is distinctly different from PS-core−PNIPAM-shell and core−shell microgel systems.[39,41,42]

Furthermore, the structure of the core−shell microgel is compared to the corresponding hollow spheres. We could show that the careful choice of the polymer thickness and connectivity can be used to tailor hollow particles with controlled void volumes and shell structures. SANS provided unique information on the structure of the particles, which is not accessible by means of electron microscopy or dynamic light scattering. Radial density profiles were obtained from an advanced form factor model. They clearly show that the void is formed, but it is predominantly filled with polymer from the shell. Hence, the "free" volume in the particle center is strongly reduced compared to the initial volume of the silica template. A higher cross-linking density can restrict the intrusion of the shell polymer into the void after core dissolution. Then, however, the temperature sensitivity of the capsule wall is nearly lost. These findings illustrate the structure-sensitivity dilemma of responsive hollow nanogels and have to be considered if temperature-sensitive polymer based delivery systems shall be tailored.

■ ASSOCIATED CONTENT

Supporting Information

Figure S1 and Table S1. This material is available free of charge via the Internet at http://pubs.acs.org.

■ AUTHOR INFORMATION

Corresponding Author

*E-mail richtering@rwth-aachen.de (W.R.).

Notes

The authors declare no competing financial interest.

■ ACKNOWLEDGMENTS

M.K. acknowledges financial support from the Fonds der Chemischen Industrie (FCI) via the Verband der Chemischen Industrie (VCI). M.K. and T.H. are grateful for financial support of the Deutsche Forschungsgemeinschaft through the SFB 840 (TP B5). J.D. and W.R. gratefully acknowledge financial support from the SFB 985 "Functional Microgels and Microgel Systems".

■ REFERENCES

(1) Mura, S.; Nicolas, J.; Couvreur, P. *Nat. Mater.* **2013**, *12* (11), 991−1003.

(2) Amstad, E.; Kim, S.-H.; Weitz, D. A. *Angew. Chem., Int. Ed.* **2012**, *51* (50), 12499−12503.

(3) Wang, Y.; Bansal, V.; Zelikin, A. N.; Caruso, F. *Nano Lett.* **2008**, *8* (6), 1741−1745.

(4) Datta, S. S.; Abbaspourrad, A.; Amstad, E.; Fan, J.; Kim, S. H.; Romanowsky, M.; Shum, H. C.; Sun, B.; Utada, A. S.; Windbergs, M. *Adv. Mater.* **2014**, *26* (14), 2205−2218.

(5) Windbergs, M.; Zhao, Y.; Heyman, J.; Weitz, D. A. *J. Am. Chem. Soc.* **2013**, *135* (21), 7933−7937.

(6) Cohen Stuart, M. A.; Huck, W. T. S.; Genzer, J.; Muller, M.; Ober, C.; Stamm, M.; Sukhorukov, G. B.; Szleifer, I.; Tsukruk, V. V.; Urban, M.; Winnik, F.; Zauscher, S.; Luzinov, I.; Minko, S. *Nat. Mater.* **2010**, *9* (2), 101−113.

(7) Skorb, E. V.; Möhwald, H. *Adv. Mater.* **2013**, *25* (36), 5029−5043.

(8) Karamitros, C. S.; Yashchenok, A. M.; Möhwald, H.; Skirtach, A. G.; Konrad, M. *Biomacromolecules* **2013**, *14* (12), 4398−4406.

(9) Caruso, F.; Trau, D.; Möhwald, H.; Renneberg, R. *Langmuir* **2000**, *16* (4), 1485−1488.

(10) Clarke, K. C.; Douglas, A. M.; Brown, A. C.; Barker, T. H.; Lyon, L. A. *Curr. Opin. Colloid Interface Sci.* **2013**, *18* (5), 393−405.

(11) Kabanov, A. V.; Vinogradov, S. V. *Angew. Chem., Int. Ed.* **2009**, *48* (30), 5418−5429.

(12) Shah, R. K.; Kim, J.-W.; Agresti, J. J.; Weitz, D. A.; Chu, L.-Y. *Soft Matter* **2008**, *4* (12), 2303−2309.

(13) Seiffert, S. *Angew. Chem., Int. Ed.* **2013**, *52* (44), 11462−11468.

(14) Chu, L.-Y.; Utada, A. S.; Shah, R. K.; Kim, J.-W.; Weitz, D. A. *Angew. Chem., Int. Ed.* **2007**, *46* (47), 8970−8974.

(15) Qin, D.; Xia, Y.; Whitesides, G. M. *Nat. Protoc.* **2010**, *5* (3), 491−502.

(16) Johnston, A. P. R.; Cortez, C.; Angelatos, A. S.; Caruso, F. *Curr. Opin. Colloid Interface Sci.* **2006**, *11* (4), 203−209.

(17) Richardson, J. J.; Ejima, H.; Lörcher, S. L.; Liang, K.; Senn, P.; Cui, J.; Caruso, F. *Angew. Chem., Int. Ed.* **2013**, *52* (25), 6455−6458.

(18) De Geest, B. G.; Sanders, N. N.; Sukhorukov, G. B.; Demeester, J.; De Smedt, S. C. *Chem. Soc. Rev.* **2007**, *36* (4), 636−649.

(19) Yang, S. Y.; Lee, D.; Cohen, R. E.; Rubner, M. F. *Langmuir* **2004**, *20* (14), 5978−5981.

(20) Zelikin, A. N.; Quinn, J. F.; Caruso, F. *Biomacromolecules* **2006**, *7* (1), 27−30.

(21) Lee, H.; Mensire, R.; Cohen, R. E.; Rubner, M. F. *Macromolecules* **2011**, *45* (1), 347−355.

(22) Karg, M.; Wellert, S.; Prevost, S.; Schweins, R.; Dewhurst, C.; Liz-Marzán, L. M.; Hellweg, T. *Colloid Polym. Sci.* **2010**, *289* (5−6), 699−709.

(23) Stöber, W.; Fink, A.; Bohn, E. *J. Colloid Interface Sci.* **1968**, *26* (1), 62−69.

(24) Zha, L. S.; Zhang, Y.; Yang, W. L.; Fu, S. K. *Adv. Mater.* **2002**, *14* (15), 1090−1092.

(25) Nolan, C. M.; Gelbaum, L. T.; Lyon, L. A. *Biomacromolecules* **2006**, *7* (10), 2918−2922.

(26) Nayak, S.; Gan, D.; Serpe, M. J.; Lyon, L. A. *Small* **2005**, *1* (4), 416−421.

(27) Lapeyre, V.; Renaudie, N.; Dechezelles, J.-F.; Saadaoui, H.; Ravaine, S.; Ravaine, V. *Langmuir* **2009**, *25* (8), 4659−4667.

(28) Zhang, F.; Hou, G.; Dai, S.; Lu, R.; Wang, C. *Colloid Polym. Sci.* **2012**, *290* (13), 1341−1346.
(29) Snowden, M. J.; Chowdhry, B. Z.; Vincent, B.; Morris, G. E. *J. Chem. Soc., Faraday Trans.* **1996**, *92* (24), 5013−5016.
(30) Berndt, I.; Richtering, W. *Macromolecules* **2003**, *36* (23), 8780−8785.
(31) Debord, J. D.; Lyon, L. A. *Langmuir* **2003**, *19* (18), 7662−7664.
(32) Pelton, R. H.; Chibante, P. *Colloids Surf.* **1986**, *20* (3), 247−256.
(33) Dubbert, J.; Nothdurft, K.; Karg, M.; Richtering, W. *Macromol. Rapid Commun.* 2014, accepted; DOI: 10.1002/marc.201400495.
(34) Masoud, H.; Alexeev, A. *ACS Nano* **2011**, *6* (1), 212−219.
(35) Putnam, D. *Nat. Mater.* **2006**, *5* (6), 439−451.
(36) Karg, M.; Pastoriza-Santos, I.; Liz-Marzán, L. M.; Hellweg, T. *ChemPhysChem* **2006**, *7* (11), 2298−2301.
(37) Xing, Z.; Wang, C.; Yan, J.; Zhang, L.; Li, L.; Zha, L. *Soft Matter* **2011**, *7* (18), 7992−7997.
(38) Serizawa, T.; Wakita, K.; Kaneko, T.; Akashi, M. *J. Polym. Sci., Part A: Polym. Chem.* **2002**, *40* (23), 4228−4235.
(39) Berndt, I.; Pedersen, J. S.; Richtering, W. *J. Am. Chem. Soc.* **2005**, *127* (26), 9372−9373.
(40) NCNR; http://www.ncnr.nist.gov/resources/activation/ (28.07.2014).
(41) Dingenouts, N.; Seelenmeyer, S.; Deike, I.; Rosenfeldt, S.; Ballauff, M.; Lindner, P.; Narayanan, T. *Phys. Chem. Chem. Phys.* **2001**, *3* (7), 1169−1174.
(42) Berndt, I.; Pedersen, J. S.; Richtering, W. *Angew. Chem.* **2006**, *118* (11), 1769−1773.
(43) Stieger, M.; Richtering, W.; Pedersen, J. S.; Lindner, P. *J. Chem. Phys.* **2004**, *120* (13), 6197−6206.
(44) Wu, X.; Pelton, R. H.; Hamielec, A. E.; Woods, D. R.; McPhee, W. *Colloid Polym. Sci.* **1994**, *272* (4), 467−477.
(45) Guillermo, A.; Cohen Addad, J. P.; Bazile, J. P.; Duracher, D.; Elaissari, A.; Pichot, C. *J. Polym. Sci., Part B: Polym. Phys.* **2000**, *38* (6), 889−898.
(46) Dong, W.-F.; Ferri, J. K.; Adalsteinsson, T.; Schönhoff, M.; Sukhorukov, G. B.; Möhwald, H. *Chem. Mater.* **2005**, *17* (10), 2603−2611.
(47) Cheng, C.-J.; Chu, L.-Y.; Ren, P.-W.; Zhang, J.; Hu, L. *J. Colloid Interface Sci.* **2007**, *313* (2), 383−388.
(48) Zhang, Y.; Jiang, M.; Zhao, J.; Ren, X.; Chen, D.; Zhang, G. *Adv. Funct. Mater.* **2005**, *15* (4), 695−699.
(49) Zhu, D.; Wang, F.; Gao, C.; Xu, Z. *Front. Chem. Eng. China* **2008**, *2* (3), 253−256.
(50) Zhang, F.; Wang, C. *Colloid Polym. Sci.* **2008**, *286* (8−9), 889−895.
(51) Qian, J.; Wu, F. *Chem. Mater.* **2007**, *19* (24), 5839−5841.
(52) Wu, S.; Dzubiella, J.; Kaiser, J.; Drechsler, M.; Guo, X.; Ballauff, M.; Lu, Y. *Angew. Chem., Int. Ed.* **2012**, *51* (9), 2229−2233.
(53) Pelton, R. *Adv. Colloid Interface Sci.* **2000**, *85*, 1−33.
(54) Senff, H.; Richtering, W. *Colloid Polym. Sci.* **1999**, *278* (9), 830−840.
(55) Berndt, I.; Pedersen, J. S.; Lindner, P.; Richtering, W. *Langmuir* **2005**, *22* (1), 459−468.
(56) Seiffert, S.; Thiele, J.; Abate, A. R.; Weitz, D. A. *J. Am. Chem. Soc.* **2010**, *132* (18), 6606−6609.
(57) Deng, J.; Yu, Y.; Dun, S.; Yang, W. *J. Phys. Chem. B* **2010**, *114* (8), 2593−2601.
(58) Kim, S.-H.; Park, J.-G.; Choi, T. M.; Manoharan, V. N.; Weitz, D. A. *Nat. Commun.* **2014**, *5*, 3068.